nature materials

Supplementary information

https://doi.org/10.1038/s41563-025-02461-x

Nonlinear phase-matched van der Waals crystals integrated on optical fibres

In the format provided by the authors and unedited

CONTENTS

Supplementary Figure 1 | Theoretical calculation of polarization dependence of SHG intensity in rBN and lithium niobate (LN)

Supplementary Figure 2 | Transmittance of fibre/rBN/fibre structure under varying crystal thickness

Supplementary Figure 3 | Homemade in-situ twist fibre transfer system

Supplementary Figure 4 | Nonlinear spectral comparison between rBN-integrated fibre and bare fibre

Supplementary Figure 5 | AFM characterization of rBN thickness

Supplementary Figure 6 | Illustration of the physical picture of global optimization ($N = 5, t = 0.4L_c$) and quasi-phase-matching ($N = 2, t = L_c$)

Supplementary Figure 7 | Numerical calculation of thickness and angular deviation effects on the local and global optimization schemes

Supplementary Figure 8 | Refractive index dispersion curve and coherence length at different excitation wavelengths

Supplementary Figure 9 | Schematic diagram of encapsulating twisted rBN between two fibres

Supplementary Figure 10 | Photo of the integrated twisted rBN optical fibre excited by 1064 nm incident light

Supplementary Figure 11 | Working bandwidth of twisted rBN integrated fibres

Supplementary Figure 12 | Twisted rBN/graphene heterostructure integrated on fibre end facet

Supplementary Figure 13 | Optical spectra of FW and SHG emitted by all-fibre SHG pulsed laser

Supplementary Figure 14 | Autocorrelation of direct output from all-fibre pulsed SHG laser based on the heterostructure integrated fibre

Supplementary Note 1: Theoretical calculation of SHG conversion efficiency of rBN flakes

Supplementary Note 2a: SHG output intensities and the stacking twist angle strategy in two flakes

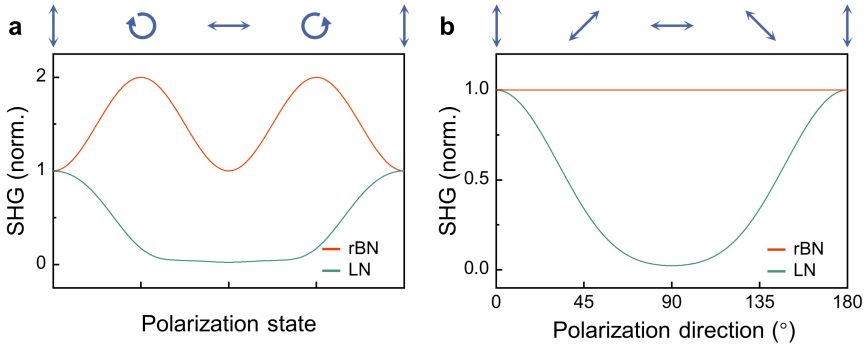
Supplementary Note 2b: Proof of the twist angle is only 0° or 60° when stacked flake by flake

Supplementary Note 3: Stacking sequence of local optimization in thickness of $\boldsymbol{t}$

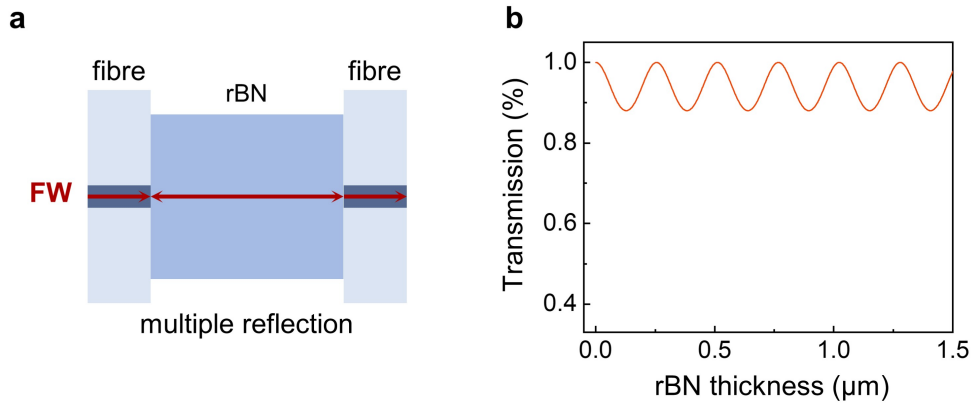
Supplementary Table 1 | Comparison of photon-pair generation via fibre end facet SPDC and various fibre FWM schemes

Supplementary Table 2 | Comparison of optical fibre based SHG devices

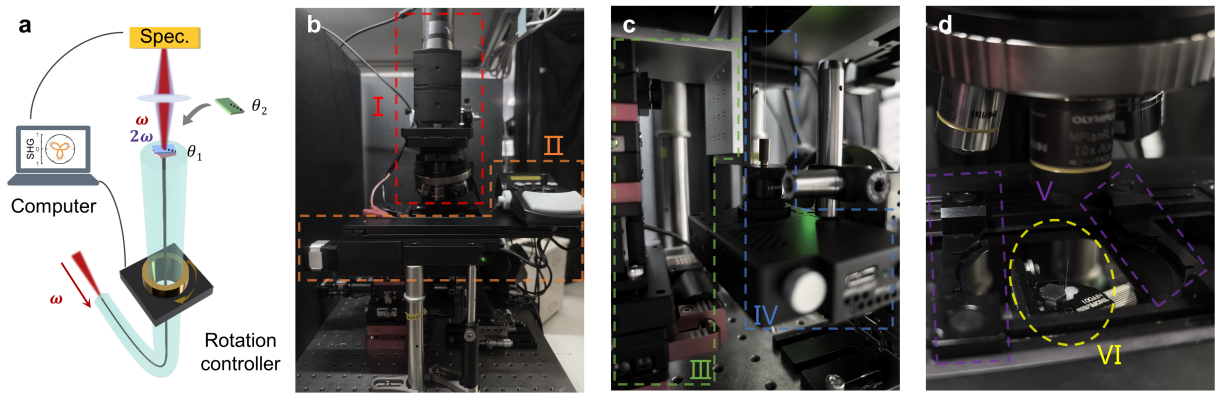
Reference



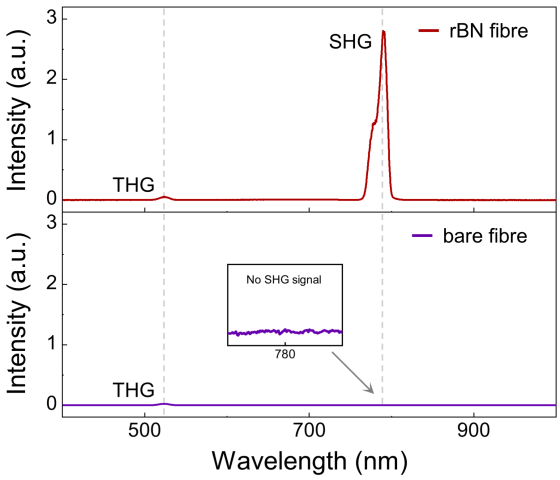
Supplementary Figure 1 | Theoretical calculation of polarization dependence of SHG intensity in rBN and lithium niobate (LN). a, Evolution of SHG intensities with the FW polarization state (ellipticity) traverses from linear to circular. **b,** Evolution of SHG intensities with the direction of linear polarization of FW in rBN and LN. Both two figures are normalized to the SHG intensity under vertically polarized laser excitation.



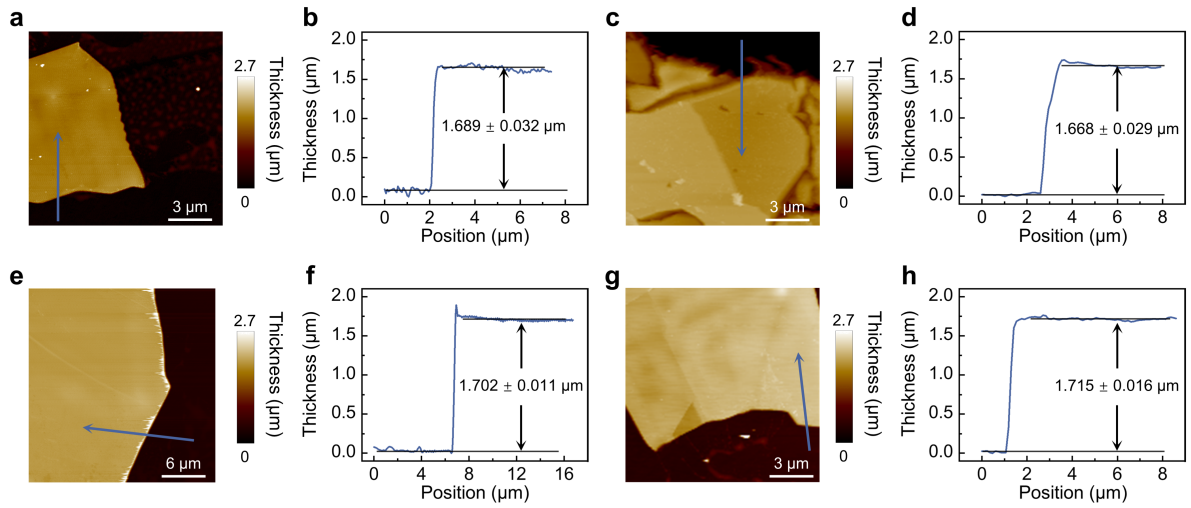
Supplementary Figure 2 | Transmittance of fibre/rBN/fibre structure under varying crystal thickness. a, Schematic of the sandwich structure of vdW crystals embedded between two fibres. **b,** Calculated transmittance as a function of rBN thickness.



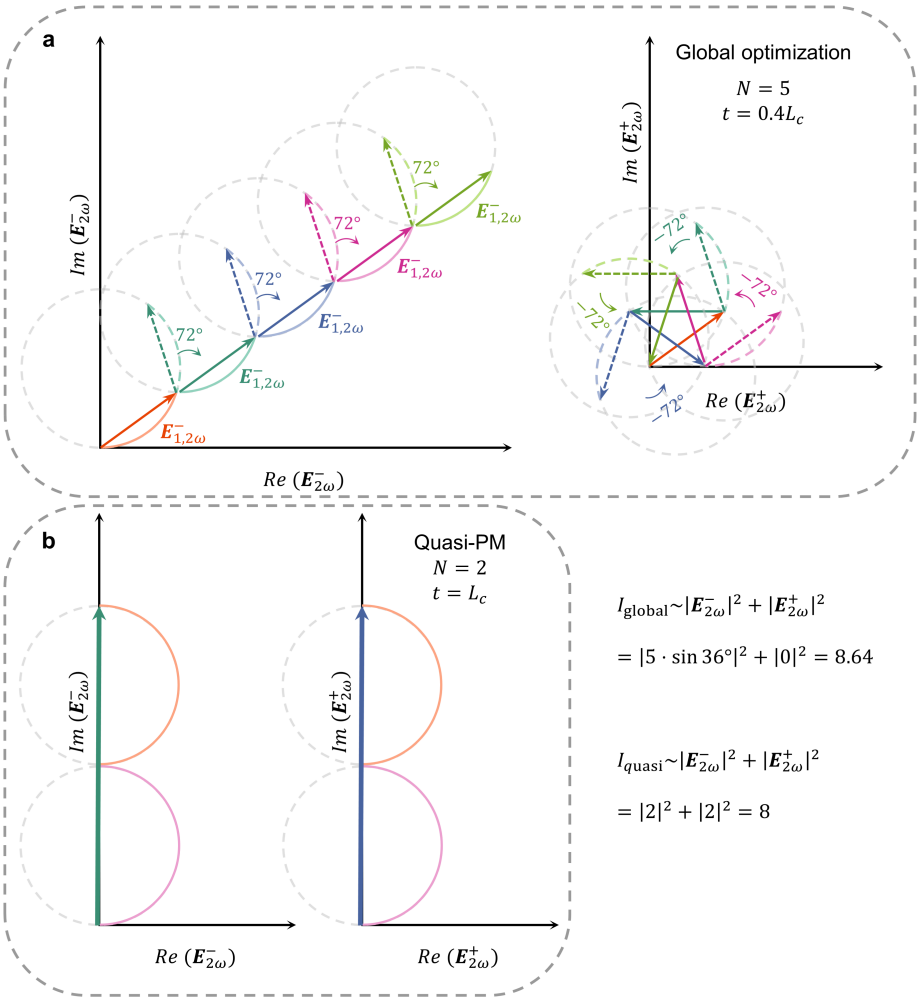
Supplementary Figure 3 | Homemade *in-situ* twist fibre transfer system. a, Schematic diagram of the system. The incident light of ω is transported through optical fibre and interacts with the rBN flakes. Generated SHG signal 2ω is collected and detected by a spectrometer. The relative twist angle between rBN flakes is controlled by a rotation motor with SHG intensity monitoring. **b,** Front view of the main setup. I: Thorlabs Cerna®-based cage system, used for imaging, collecting signals through the objective into the spectrometer. II: A Prior motorized XY stage (ProScan H117E1N4) and controller, enabling precise planar (XY) movement of the upper-flake material to be transferred. **c,** Detailed view from underneath. III: A custom five-axis translation stage, used to hold, spatially move and tilt the optical fibre. IV: A three-axis translation stage combined with Thorlabs' K10CR2/M Stepper Motor Rotation Mount, providing coaxial rotation of the fibre for twist experiments. **d,** Detailed view from above. V: A dedicated fixture mounted on the Prior stage, used to secure the holder of the upper-flake material. VI: A fibre clamp assembly, designed to keep the fibre firmly in place.



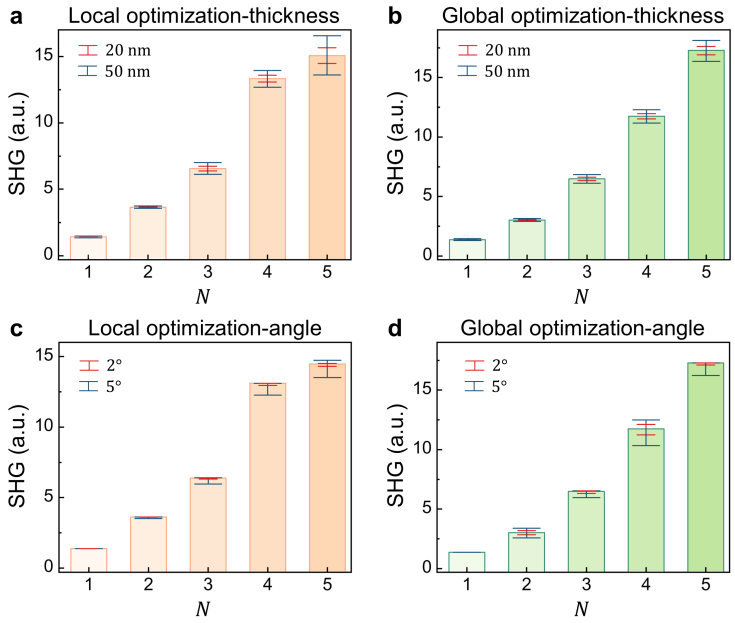
Supplementary Figure 4 | Nonlinear spectral comparison between rBN-integrated fibre and bare fibre. Using a 1560 nm pulsed fibre laser as the excitation source, the laser (peak intensity of 2 GW/cm^2) is coupled into the encapsulated fibre/rBN/fibre device. A strong SHG peak at ~780 nm is observed, along with a weak third-harmonic (THG) signal at ~520 nm (top panel). Under the same condition, the bare fibre (bottom panel) shows only a weak THG signal generated with ~1 m length, without any detectable SHG. The inset zoomed-in the spectral region near 780 nm, confirming the absence of SHG in the bare fibre.



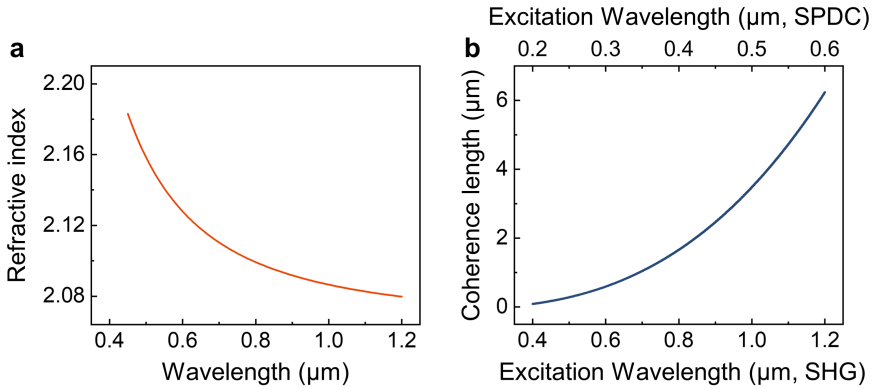
Supplementary Figure 5 | AFM characterization of rBN thickness. a, c, e, and g, AFM mapping images of rBN flakes. **b, d, f, and h,** the corresponding height profiles measured along the blue arrows. Across these samples, the thickness fluctuation remains within 2%.



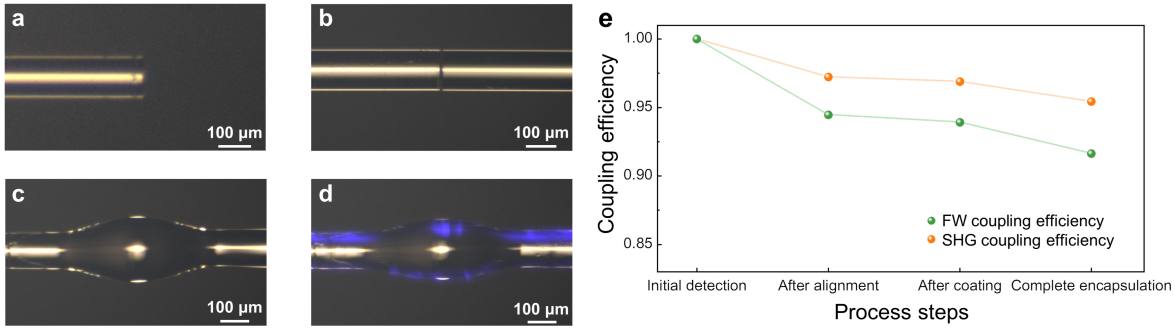
Supplementary Figure 6 | Illustration of the physical picture of global optimization ($N = 5, t = 0.4L_c$) and quasi-phase-matching ($N = 2, t = L_c$). a, Effect of linearly polarized excitation is divided into two circular components ($E^-$and E^+). The equal-magnitude orange, sage green, blue, magenta and earthy green vector represents the five flakes in sequence. For this certain situation, the left circularly polarized component ($E^-_{2\omega}$) is maximized through rotation angle serials leaving a minimum $E^+_{2\omega} = 0$. **b,** In Quasi-PM, the twisted angle between the layers is 60°. Under these conditions, the SHG intensity of two circular components ($E^-_{2\omega}$ and $E^+_{2\omega}$) are equal. Assume the length corresponding to L_c (the diameter of the circle) is 1, the calculated SHG intensities I_{global} and I_{quasi} are 8.64 and 8, respectively.



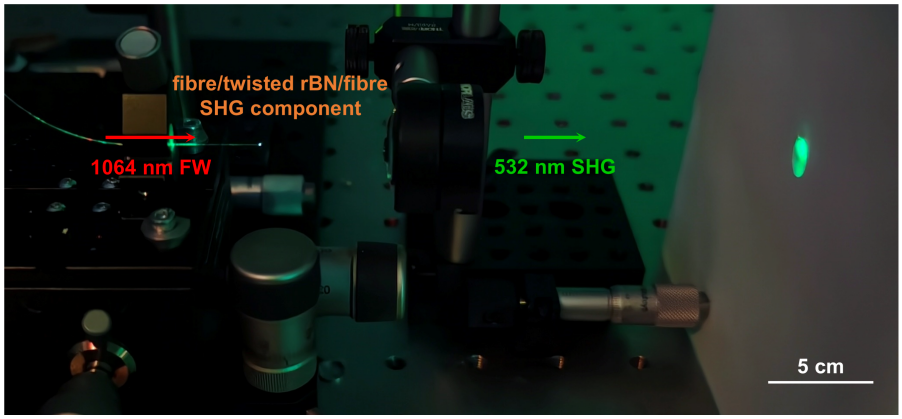
Supplementary Figure 7 | Numerical calculation of thickness and angular deviation effects on the local and global optimization schemes. a, Calculated SHG for the local optimization $(0°, 0°, 60°, 60°, 0°)$ with each flake $(0.4L_c = 1.7\ \mu m)$ contributing a thickness deviation (pink error bars represent the minimum and maximum of 40 points uniformly sampled from –20 nm to +20 nm, and blue error bars represent the minimum and maximum of 100 points uniformly sampled from –50 nm to +50 nm). **b,** Corresponding calculations for the global optimization $(0°, 24°, 48°, 72°, 96°)$ approach under the same deviation conditions. **c,** Calculated SHG for the local optimization with each flake contributing an angular deviation (pink error bars represent the minimum and maximum of 40 points uniformly sampled from –2° to +2°, and blue error bars represent the minimum and maximum of 100 points uniformly sampled from –5° to +5°). **d,** Corresponding calculations for the global optimization approach under the same deviation conditions. The error bars highlight how small thickness and angular deviations in each flake influence the overall second-harmonic response.



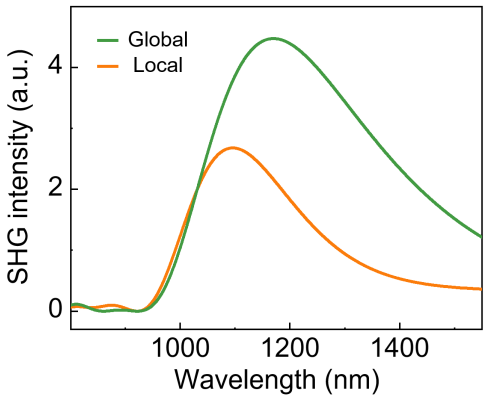
Supplementary Figure 8 | Refractive index dispersion curve and coherence length at different excitation wavelengths. a, Dispersion of the refractive index for BN (ref. 45). **b,** The coherence length at different excitation wavelengths for SHG and SPDC processes in rBN is calculated according to the refractive index dispersion.



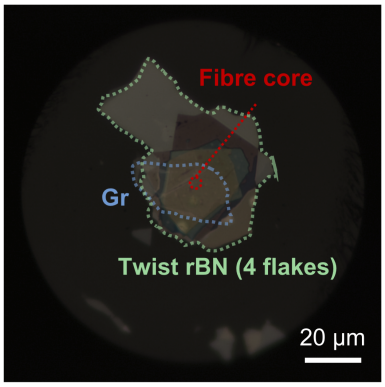
Supplementary Figure 9 | Schematic diagram of encapsulating twisted rBN between two fibres. a, Fix the fibre on the left side, connect the laser, and directly detect the incident power**. b,** Align two fibres using multi-axis stages to achieve a maximum transmittance. **c,** UV curing resin coating. **d,** UV light curing encapsulation. **e,** FW and SHG coupling efficiency at different steps. In total < 10% insertion loss can be observed.



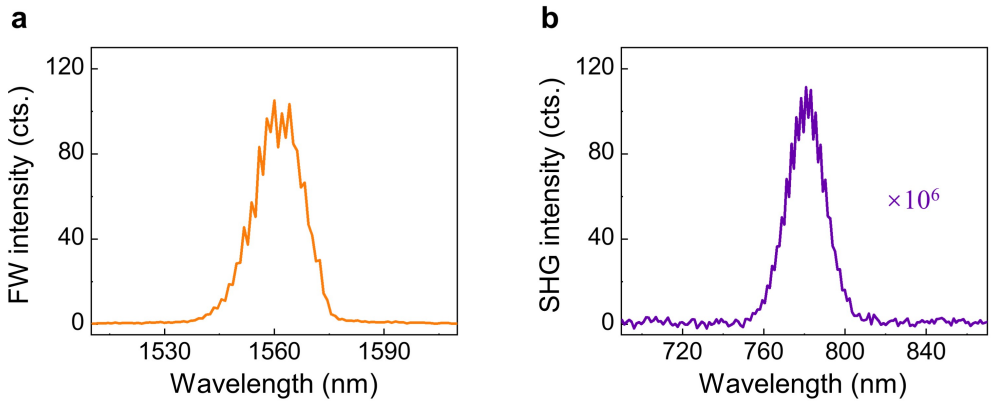
Supplementary Figure 10 | Photo of the integrated twisted rBN optical fibre excited by 1064 nm incident light. The excitation light is coupled into the optical fibre by the Nikon objective (20 ×, NA=0.30). Twisted rBN at the output end of the fibre generates a bright SHG (532 nm) beam.



Supplementary Figure 11 | Working bandwidth of twisted rBN integrated fibres. Considering the chromatic dispersion of rBN at different wavelengths and the corresponding coherence length, the global and local optimization fibre with a total thickness of 8.5 μm ($2L_c$ of 1064 nm) are calculated, where the green line is the global optimization, and the orange line is the local optimization.

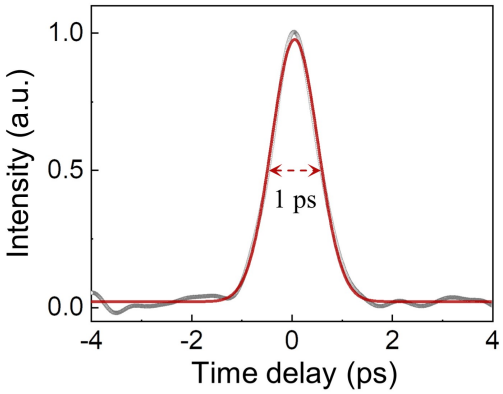


Supplementary Figure 12 | Twisted rBN/graphene heterostructure integrated on fibre end facet. Optical image of 10-layer graphene and 4 flakes twisted rBN on the fibre end facet.



Supplementary Figure 13 | Optical spectra of FW and SHG emitted by all-fibre SHG pulsed laser. a, FW signal at 1560 nm with FWHM (full width at half maximum) of 16 nm. b, SHG signal at 780 nm with FWHM of 23 nm.

125



Supplementary Figure 14 | Autocorrelation of direct output from all-fibre pulsed SHG laser based on the heterostructure integrated fibre. Autocorrelation trace without DCF compression with FWHM of ~1 ps fitted by a Gaussian function, corresponding to a pulse duration of ~0.7 ps.

Supplementary Note 1: Theoretical calculation of SHG conversion efficiency of rBN flakes

Here, we employ the coupling wave equations in the slowly varying amplitude approximation as follows (we assume the light propagates along the z-axis):

$$\begin{cases} \frac{\partial \boldsymbol{A}(2\omega)}{\partial z} = \frac{i2\omega}{2\varepsilon_0 cn(2\omega)} \boldsymbol{P_{NL}}(\boldsymbol{K_2}, 2\omega) e^{-i(k(2\omega)z - 2\omega t)} \\ \frac{\partial \boldsymbol{A}(\omega)}{\partial z} = \frac{i2\omega}{2\varepsilon_0 cn(\omega)} \boldsymbol{P_{NL}}(\boldsymbol{K_2}, \omega) e^{-i(k(\omega)z - \omega t)} \end{cases} \quad \text{(S1)}$$

where $\boldsymbol{A}$, c, n, $\boldsymbol{P_{NL}}$ and k represent the complex amplitude of electric field, the light speed in vacuum, the refractive index, the nonlinear polarization and the wavevector, respectively. The up and down panels in Equation (S1) are for the fundamental and second harmonic waves, respectively, $\boldsymbol{P_{NL}}(\boldsymbol{K_2}, 2\omega)$ can be expressed as

$$\boldsymbol{P_{NL}}(\boldsymbol{K_2}, 2\omega) = \boldsymbol{P^{(2)}}(2\omega) = \varepsilon_0 \chi^{(2)}(-2\omega, \omega, \omega) : \boldsymbol{E}(\omega)\boldsymbol{E}(\omega). \quad \text{(S2)}$$

For rBN, the second-order nonlinear susceptibility tensor χ_{ijk} can be written as

$$\begin{bmatrix} 0 & 0 & 0 & 0 & \chi_{15} & -\chi_{22} \\ -\chi_{22} & \chi_{22} & 0 & \chi_{15} & 0 & 0 \\ \chi_{31} & \chi_{31} & \chi_{33} & 0 & 0 & 0 \end{bmatrix}. \quad \text{(S3)}$$

Since the polarization of fundamental wave is in the xy-plane, we ignore the z-component, and the non-vanishing tensor elements are

$$\chi^{(2)} = \chi_{yyy} = -\chi_{xyx} = -\chi_{yxx} = -\chi_{xxy}. \quad \text{(S4)}$$

Where the armchair and zigzag directions lie along the x and y coordinates, respectively. Thus, the second-order polarization can be written as $P_x = \varepsilon_0 \chi^{(2)}\left(E_x^2 - E_y^2\right), P_y = -2\varepsilon_0 \chi^{(2)} E_x E_y$. To facilitate calculation, we perform coordinate transformation in this article, as following, $\boldsymbol{P} = (P_-, P_+)^T = \left(P_x - iP_y, P_x + iP_y\right)^T/\sqrt{2}$, $\boldsymbol{E} = (E_-, E_+)^T = \left(E_x - iE_y, E_x + iE_y\right)^T/\sqrt{2}$.

Considering the undepleted pump approximation, which means to ignore the second equation in Equation (S1) and let $\boldsymbol{A}(\omega)$ be constant, we finally get the intensity of the SHG (T is the thickness of rBN and $I_{in}(\omega)$ is the intensity of the fundamental wave) as

$$I(2\omega) = \frac{2\omega^2}{c^3\varepsilon_0 n^2(\omega)\mathrm{n}(2\omega)}\left(\chi^{(2)}\right)^2 I^2(\omega)T^2\frac{\sin^2\left(\frac{\Delta kT}{2}\right)}{\left(\frac{\Delta kT}{2}\right)^2}. \quad \text{(S5)}$$

And the SHG conversion efficiency is expressed as

$$\eta_{SHG} = \frac{I_{out}(2\omega)}{I_{in}(\omega)} = \frac{2\omega^2}{c^3\varepsilon_0 n^2(\omega)n(2\omega)}\left(\chi^{(2)}\right)^2 I_{in}(\omega)T^2\frac{\sin^2\left(\frac{\Delta kT}{2}\right)}{\left(\frac{\Delta kT}{2}\right)^2}. \quad \text{(S6)}$$

With the measured nonlinear coefficient $\chi^{(2)}$ of rBN as about 30 pm V^{-1}, the theoretical conversion efficiency is ultimate obtained to be 1.6% at a coherence length (4.25 μm) of 1064 nm excitation light. For quasi-phase-matching, the theoretical value of the conversion efficiency at twice the coherence length (8.5 μm) is 6.4%.

Supplementary Note 2a: SHG output intensities and the stacking twist angle strategy in two flakes.

In this Note, we define I_n^-,(I_n^+), and E_n^-,(E_n^+) are the left (right) circularly polarized SHG intensity and optical electric field strength in the **single n^{th} flake**. $I_{\sum}{}_n^-$,($I_{\sum}{}_n^+$), and $E_{\sum}{}_n^-$,($E_{\sum}{}_n^+$) are the left (right) circularly polarized SHG optical field and electric intensities in the **total n flake.**

So, the electric field and optical field intensities of SHG in two flakes can be expressed as

$$I_{1+2} = I_{1+2}^- + I_{1+2}^+ \tag{S7}$$

$$I_{1+2}^{\pm} \propto \left|\boldsymbol{E}_{1+2}^{\pm}\right|^2 \tag{S8}$$

According to the geometry as demonstrated in Fig. 2b and cosine theorem, the electric field intensity of SHG can be expressed as

$$\left|\boldsymbol{E}_{1+2}^{\pm}\right|^2 = \left|\boldsymbol{E}_1^{\pm}\right|^2 + \left|\boldsymbol{E}_2^{\pm}\right|^2 - 2\cdot\left|\boldsymbol{E}_1^{\pm}\right|\cdot\left|\boldsymbol{E}_2^{\pm}\right|\cdot\cos(\alpha \pm 3\theta) \tag{S9}$$

Based on the trigonometric function and angle formula, we can get

$$\left|\boldsymbol{E}_{1+2}^{\pm}\right|^2 = \left|\boldsymbol{E}_1^{\pm}\right|^2 + \left|\boldsymbol{E}_2^{\pm}\right|^2 - 2\cdot\left|\boldsymbol{E}_1^{\pm}\right|\cdot\left|\boldsymbol{E}_2^{\pm}\right|(\cos(\alpha)\cos(3\theta) \mp \sin(\alpha)\sin(3\theta)) \tag{S10}$$

Where α is the angle between the $\boldsymbol{E}_1$ and $\boldsymbol{E}_2$ vectors when there is no twist, θ is the twist angle of the first flake and the second flake. Since $\left|\boldsymbol{E}_{1,2}^-\right| = \left|\boldsymbol{E}_{1,2}^+\right|$, we can according to $(\mathrm{S8}-10)$ simplify (S7) to the following formula.

$$I_{1+2} \propto -\cos(\alpha)\cos(3\theta) \tag{S11}$$

When the two flakes' total thickness is fixed, the value of α is also determined accordingly. When $\alpha > 90°$, the angle between the $\boldsymbol{E}_1$ and $\boldsymbol{E}_2$ vectors are obtuse, $\cos(\alpha)$ is a negative value, when θ is 0°, I takes the maximum value. Similarly, when $\alpha < 90°$, when θ is 60°, I takes the maximum value.

Supplementary Note 2b: Proof of the twist angle is only 0° or 60° when stacked flake by flake.

For this part, we use mathematical induction to prove. First, we prove that the twist angle θ_1 must be 0° or 60° when the two flakes, which has been proved in Supplementary Note 2a. Then we assume that for any flakes $n \geq 2$, the twist angle θ_n is 0° or 60°， which physical expression is the θ_n between the total vector of the n flakes $\boldsymbol{E}_{\sum n-1}$ and the n^{th} flake $\boldsymbol{E}_n$ is 0° or 60°. With the assumption of the Induction Hypothesis in hand, we conclude that the SHG electric field intensity when the $n+1$ flake is the following

$$\left|\boldsymbol{E}^{\pm}_{\sum n+1}\right|^2 = \left|\boldsymbol{E}^{\pm}_{\sum n}\right|^2 + \left|\boldsymbol{E}^{\pm}_{n+1}\right|^2 \tag{S12}$$

Similar to Supplementary Note 2a, according to the cosine theorem and trigonometric function and angle formula, we can get the electric field intensity to be

$$I^{\pm}_{\sum n+1} = \left|\boldsymbol{E}^{\pm}_{\sum n}\right|^2 + \left|\boldsymbol{E}^{\pm}_{n+1}\right|^2 - 2 \cdot \left|\boldsymbol{E}^{\pm}_{\sum n}\right| \cdot \left|\boldsymbol{E}^{\pm}_{n+1}\right| (\cos(\alpha_{n+1}) \cos(3\theta_{n+1}) \mp \sin(\alpha_{n+1}) \sin(3\theta_{n+1})) \tag{S13}$$

Where α_{n+1} is the angle between the $\boldsymbol{E}_{\sum n}$ and $\boldsymbol{E}_{n+1}$ vectors when there is no twist, θ_{n+1} is the twist angle between the total vector of the n flakes $\boldsymbol{E}_{\sum n-1}$ and the n^{th} flake $\boldsymbol{E}_n$, which is 0° or 60°, we can get $\left|\boldsymbol{E}^{-}_{\sum n}\right| = \left|\boldsymbol{E}^{+}_{\sum n}\right|$. In addition, $|\boldsymbol{E}^{-}_{n+1}| = |\boldsymbol{E}^{+}_{n+1}|$, we can simplify (S12) to the following formula

$$I_{\sum n+1} \propto -\cos(\alpha_{n+1}) \cos(3\theta_{n+1}) \tag{S14}$$

According to the angle of α_{n+1} we can get the maximum intensity in θ_{n+1} at 0° or 60°. In summary, we can get that for any n, θ_n is only 0° or 60° to get maximum SHG intensity.

Supplementary Note 3: Stacking sequence of local optimization in thickness of t.

The stacking sequence of local optimization can be summarized as $\{N_1, N_2, \cdots, N_q\}$, This is an increasing sequence and each item is a positive integer, each item in it represents which flake needs to have a twist angle of 60° relative to the previous flake. For the thickness t of each flake, the sequence $\{N_q\}$ can be obtained recursively according to the following inequality, for each N, ensure that it takes the smallest integer that can be obtained, and $N_1 \geq 2$.

According to the above description, we can get that if there are no twist angle in the first $N-1$ flakes, and there is(isn't) a relative twist angle for the N^{th} flake, the SHG intensity is as follows

$$I_q^{twist} = A^2 \cdot \left(2 \cdot \left| \sum_{i=1}^{N-1} \left(e^{-i\Delta k z_i} \right) - e^{-i\Delta k z_N} \right|^2 \right) \tag{S15}$$

$$I_q^{no\ twist} = A^2 \cdot \left(2 \cdot \left| \sum_{i=1}^{N} \left(e^{-i\Delta k z_i} \right) \right|^2 \right) \tag{S16}$$

Where $A = \frac{\sqrt{2}\omega\chi}{-cn(2\omega)\Delta k} E_0^2 \left(1 - e^{-i\Delta k t}\right)$, E_0 is the incident light intensity along the x direction, z_i is the coordinates of the i^{th} flake. Simplifying the above formula, we can get the position N of the first twist angle that satisfies

$$\left| 1 - 2e^{-i\Delta k(N-1)t} + e^{-i\Delta k N t} \right| \geq \left| 1 - e^{-i\Delta k N t} \right| \tag{S17}$$

Following the first flake, we can obtain the $\{N_q\}$ from the following inequality

$$\left| 1 + 2 \sum_{p=1}^{p=q} e^{-i\Delta k (N_p - 1)t} \cdot (-1)^p - e^{-i\Delta k N_q t} \right| \geq \left| 1 + 2 \sum_{p=1}^{p=q-1} e^{-i\Delta k (N_p - 1)t} \cdot (-1)^p + e^{-i\Delta k N_q t} \right| \tag{S18}$$

For example, when $t = L_c$, we can get the sequence $\{2,3,4,\cdots\}$, which means each flake, starting from the second flake, needs to have a relative twist angle with the previous flake. when $t = 0.5L_c$, we can get the sequence $\{2,4,6,\cdots\}$ or $\{3,5,7,\cdots\}$, which means each even(odd)-numbered flake starting from the second (third) flake needs to have a relative twist angle with the previous flake.

Table 1 | Comparison of photon-pair generation via fibre end facet SPDC and various fibre FWM schemes

	rBN fibre (This work)	**Dispersion shifted fibre**[1,2]	**Photonic crystal fibre**[3]	**Micro/nano-fibre**[4]	**Birefringent fibre**[5]
Mechanism	SPDC	FWM	FWM	FWM	FWM
Effective fibre length	~10 μm	~10-100 m	~1 m	~10 cm	~10 cm
Brightness	1×10^{-6} pair/pulse	6×10^{-1} pair/pulse	2×10^{-1} pair/pulse	3×10^{-2} pair/pulse	3×10^{-4} pair/pulse
CAR	144	30	48	530	130
Phase matching method	twist phase-matching	zero dispersion tuning	dispersion engineering	dispersion engineering	birefringent phase-matching
Detuning regime	small-detuning	small-detuning	large-detuning	large-detuning	large-detuning
Filtering method	free-space or all-fibre	free-space	free-space or all-fibre	free-space or all-fibre	free-space or all-fibre
Wavelength range	ultraviolet to infrared	telecom band	visible to telecom band	visible to telecom band	visible

Table 2 | Comparison of optical fibre based SHG devices

Device type	FW wavelength	System	SHG efficiency	Interaction length	SHG peak power density	Phase-matching bandwidth	Ref
Nonlinear crystal integrated	1064 nm	Twist phase-matching rBN integrated fibre	4.1%	8.5 μm	3.3 GW/cm^2	＞200 nm	This work
	800 nm	PCF embedded MoS_2	0.01%	25 cm	6.7×10^{-5} GW/cm^2	No phase-matching	ref [6]
	1550 nm	GaSe composite microfibre	1.6×10^{-6}	4 mm	2.5×10^{-12} GW/cm^2	~120 nm	ref [7]
Fibre material modification	1064 nm	Doped fibre (SMF)	1.5%	50 cm	$\sim7.5\times10^{-2}$ GW/cm^2	No phase-matching	ref [8]
	1064 nm	Doped fibre (MMF)	0.05%	50 cm	$\sim3.8\times10^{-2}$ GW/cm^2	No phase-matching	ref [8]
	1064 nm	Ce-doped-aluminosilicate fibre	1.5%	40 cm	2.1×10^{-2} GW/cm^2	No phase-matching	ref [9]
	1545 nm	Tellurite fibre	1.15%	2.5 m	4.4×10^{-2} GW/cm^2	No phase-matching	ref [10]
Fibre structural design	1542 nm	Periodically poled silica fibres	15%	32 cm	0.7 GW/cm^2	2.8 nm	ref [11]
	1550 nm	Chirped-period poled silica fibres	0.6%	10 cm	—	51 nm	ref [12]
	1230 nm	Tilted long period grating fibre	0.14%	5 cm	—	15 nm	ref [13]
	840 nm	Plasmon fibre cavity	1.6×10^{-5}	—	2.0×10^{-2} GW/cm^2	12 nm	ref [14]

1. Li, X., Chen, J., Voss, P., Sharping, J. & Kumar, P. All-fiber photon-pair source for quantum communications: Improved generation of correlated photons. *Opt. Express* **12**, 3737–3744 (2004).
2. Takesue, H. & Inoue, K. 1.5-μm band quantum-correlated photon pair generation in dispersion-shifted fiber: Suppression of noise photons by cooling fiber. *Opt. Express* **13**, 7832 (2005).
3. Fulconis, J., Alibart, O., Wadsworth, W., Russell, P. S. J. & Rarity, J. High brightness single mode source of correlated photon pairs using a photonic crystal fiber. *Opt. Express* **13**, 7572–7582 (2005).
4. Cui, L. *et al.* Generation of correlated photon pairs in micro/nano-fibers. *Opt. Lett.* **38**, 5063 (2013).
5. Smith, B. J., Mahou, P., Cohen, O., Lundeen, J. S. & Walmsley, I. A. Photon pair generation in birefringent optical fibers. *Opt. Express* **17**, 23589 (2009).
6. Zuo, Y. *et al.* Optical fibres with embedded two-dimensional materials for ultrahigh nonlinearity. *Nat. Nanotechnol.* **15**, 987–991 (2020).
7. Jiang, B. *et al.* High-efficiency second-order nonlinear processes in an optical microfibre assisted by few-layer GaSe. *Light Sci. Appl.* **9**, 63 (2020).
8. Saifi, M. A. & Andrejco, M. J. Second-harmonic generation in single-mode and multimode fibers. *Opt. Lett.* **13**, 773–775 (1988).
9. Krol, D. M. & Simpson, J. R. Photoinduced second-harmonic generation in rare-earth-doped aluminosilicate optical fibers. *Opt. Lett.* **16**, 1650 (1991).
10. Cheng, T. *et al.* Highly efficient second-harmonic generation in a tellurite optical fiber. *Opt. Lett.* **44**, 4686 (2019).
11. Canagasabey, A. *et al.* High-average-power second-harmonic generation from periodically poled silica fibers. *Opt. Lett.* **34**, 2483–2485 (2009).
12. Canagasabey, A. *et al.* Aperiodically poled silica fibers for bandwidth control of quasi-phase-matched second-harmonic generation. *Opt. Lett.* **35**, 724 (2010).
13. Elzahaby, E. A., Kandas, I. & Aly, M. H. Second harmonic generation in thin optical fibers via cladding modes. *Opt. Express* **24**, 11435 (2016).
14. Ai, Q., Sterl, F., Zhang, H., Wang, J. & Giessen, H. Giant second harmonic generation enhancement in a high- *q* doubly resonant hybrid plasmon–fiber cavity system. *ACS Nano* **15**, 19409–19417 (2021).